Visualizing Surface Phase Separation in PS-PMMA Polymer Blends at the Nanoscale

Dušan Mrđenović,[1] Daniel Abbott,[1] Victor Mougel,[1] Weitao Su,[2] Naresh Kumar,[1] and Renato Zenobi[1*]*

1 Department of Chemistry and Applied Biosciences, ETH Zurich, CH-8093 Zurich, Switzerland.

2 School of Sciences, Hangzhou Dianzi University, 310018 Hangzhou, China

*kumar@org.chem.ethz.ch, zenobi@org.chem.ethz.ch

KEYWORDS: polymer blends, phase separation, tip-enhanced Raman spectroscopy, nanoscale imaging, nanospectroscopy

ABSTRACT: Phase-separated polymer blend films are an important class of functional materials with numerous technological applications including solar cells, catalysis, and biotechnology. These technologies are underpinned by precise control of phase separation at the nanometer length-scales, which is highly challenging to visualize using conventional analytical tools. Herein, we introduce tip-enhanced Raman spectroscopy (TERS), in combination with AFM, confocal Raman spectroscopy, and XPS, as a sensitive nanoanalytical method to determine lateral and vertical phase-separation in polystyrene (PS)-poly(methyl methacrylate) (PMMA) polymer blend films. Correlative topographical, molecular, and elemental information reveals a vertical phase separation of the polymers within the top *ca.* 20 nm of the blend surface in addition to the lateral phase separation in the bulk. Furthermore, complementary TERS and XPS measurements reveal the presence of PMMA within 9.2 nm of the surface and PS at the sub-surface of the polymer blend. This fundamental work establishes TERS as an powerful analytical tool for surface characterization of this important class of polymers at nanometer length-scales.

INTRODUCTION

In the recent years, there has been a surge of interest in polymer blend films due to their wide range of applications in display devices, solar cells, high-density information storage media, catalysis, and biotechnology.[1–6] Phase separation in polymer blends depends on various factors such as blend composition,[7] film thickness,[8] polymer solubility,[9] and substrate surface energy.[10] There are two types of phase separation in polymer blends – lateral and vertical.[11] In lateral phase

separation, polymers are stacked side by side, while in the vertical phase separation, polymers are layered on top of each other. Control of the polymer phase separation is crucial for a successful application of polymer blends in the above-mentioned technologies. For example, Li *et al.* fabricated a multilayered film of polystyrene (PS)-poly(methyl methacrylate) (PMMA) polymer block copolymer/homopolymer blends with gradually increasing refractive index and a high light transmittance, making it an excellent antireflective coating that improves performance of display devices or solar cells.[1] Budkowski *et al*. demonstrated three different types of polymer blend films suitable for electronic products and biotechnology, depending on the type of polymer phase separation.[5] Hester *et al.* fabricated a comb polymer blend of PMMA backbone and polyethylene oxide side chains in polyvinylidene fluoride, where surface segregation takes place upon annealing.[6] The annealed film demonstrated a significant protein adsorption resistance and it could be regenerated, making it an attractive material for water ultrafiltration devices.

Vertical and lateral polymer phase separation can occur at the nanometer length-scale and therefore, requires analytical tools with ultrahigh sensitivity and spatial resolution for its analysis.[12] However, conventional analytical methods for polymer characterization suffer from several limitations. For example, atomic force microscopy (AFM) provides information about polymer morphology and nanomechanical properties, but it cannot directly identify its chemical properties.[12] On the other hand, X-ray photoelectron spectroscopy (XPS) can inform about the polymer's chemistry with excellent vertical resolution (<10 nm), but the lateral resolution is limited to the micrometer scale, thus precluding determination of lateral phase separation and local distribution.[7] Spectromicroscopic techniques like Fourier-transform infrared[13] and confocal Raman microscopies[14] provide a plethora of chemical information with molecular specificity, however their spatial resolution remains diffraction-limited to the sub-micron scale. Amongst the nanoscale techniques, nanoscale secondary ion mass spectrometry is destructive and requires isotopic labelling,[15] whilst sampling depth of photothermally-induced resonance (commonly known as AFM-IR) is a few micrometers, thus having low vertical resolution and sensitivity.[16] Transmission electron microscopy (TEM) can be used to study phase separation in polymers.[17] However, it requires specialized sample preparation for e.g., embedding the sample in epoxy resin and microtoming it into thin sections. Moreover, it has limited molecular characterization ability and polymer samples can be easily charged[18] and/or damaged[19] by the electron beam.

In the last two decades, tip-enhanced Raman spectroscopy (TERS) has emerged as a label-free and non-destructive analytical tool for nanoscale surface characterization under ambient conditions by combining the high spatial resolution of scanning probe microscopy (SPM) and chemical sensitivity of surface-enhanced Raman spectroscopy.[16,20,21] In TERS, Raman signals from a nanoscopic sample volume are plasmonically enhanced by a highly intense and localized electric field, which is generated at the apex of a metallic SPM probe *via* localized surface plasmon resonance.[22–24] TERS has been successfully applied for nanoscale surface characterization of a wide variety of samples such as two-dimensional (2D) materials,[25–29] 2D reactive systems,[30–32] heterogenous catalysts,[33] organic photovoltaic devices,[34] lipid membranes[35] and biological cells.[36] However, despite the apparent suitability of TERS to probe surface chemistry at the nanoscale, its

application to study polymer blends has been surprisingly limited. The low Raman cross-section of polymeric materials in addition to the weaker enhancement in non-gap mode TERS might have been the reasons for the lack of TERS studies of polymer blends. For example, investigation of polyisoprene-PS[37] and PMMA-(PS-co-acrylonitrile) blends was attempted using TERS.[38] However, these studies provided no evidence of TERS signal enhancement and therefore, their results cannot be distinguished from confocal/far-field Raman spectroscopy. Furthermore, the TERS system stability during the duration of experiment is limited. For example, Xue *et al*.[38] recorded a single TERS image for ~91 h, which is highly undesirable for a TERS experiment since maintaining laser-probe alignment, preventing system drift, and preserving plasmonic enhancement of the TERS probe for such a long time is nearly impossible.

In this work, we employ a complementary suite of techniques to comprehensively investigate the phase separation in PS-PMMA polymer blends for the first time. It is well-known that a PS-PMMA blend consists of laterally-separated PS- and PMMA-rich phases at ambient conditions.[7,39–44] Herein, using correlative topographical, molecular, and elemental information, we demonstrate that besides the previously-observed lateral phase separation, a vertical phase separation also takes place at the top *ca.* 20 nm of the PS-PMMA blend surface. Complementary TERS and XPS measurements reveal the presence of ultrathin PMMA and PS layers at the surface and sub-surface of the polymer blend. TERS played a pivotal role in providing this information, which would have been missed with other analytical methods. This work firmly establishes TERS as a powerful analytical tool for surface polymer characterization at nanometer length-scales.

EXPERIMENTAL DETAILS

Sample preparation. PS (Molecular weight ~100 000, GPC standard) and PMMA (Molecular weight ~120 000, GPC standard) were purchased from Sigma-Aldrich, USA. Polydispersities of PS and PMMA are 1.06 and 2.2, respectively. Stock polymer solutions were prepared by dissolving each polymer in chloroform at 20 mg/mL concentration. Stock polymer solutions were mixed in 1:1 ratio (*v*/*v*), and 50 µL of a PS-PMMA mixture solution was spin-coated onto a clean glass coverslip for 3 minutes at 2500 revolutions per minute in a nitrogen atmosphere.

AFM, confocal Raman, and TERS measurements. AFM, confocal Raman, and TERS measurements were performed using a home-built instrument consisting of an inverted laser-scanning confocal microscope (IX70, Olympus, Japan), an AFM (BioScope Catalyst, Bruker, USA), a Raman spectrometer (InVia spectrometer, Renishaw, UK), and a CCD camera (DU420-EV-130, Andor, UK). An oil immersion objective lens (100×, 1.49 NA, Nikon, Japan) was used to focus a radially-polarized laser beam of 532 nm wavelength (Ventus, Laser Quantum, UK) onto a sample surface in transmission mode, as schematically illustrated in Figure 1a. The Raman scattered light was collected using the same objective and directed into the spectrometer. Prior to TERS measurements, an AFM topography image of a region of interest was recorded in PeakForce tapping mode operated with the Bruker Nanoscope software at a scan rate of 1 Hz using HQ:NSC15/Al BS (k = 40 N/m) and HQ:NSC14/No Al (k = 5 N/m) probes from MikroMasch,

Estonia. Instrument stability was checked by recording AFM images of the same PS-PMMA blend region in a time-lapse manner. AFM imaging showed a sample drift of ~8 nm/minutes (Figures S1a and S1b), which is relatively small compared to the size of scan area and polymer domains. The excitation laser was then aligned with the probe apex using hotspot imaging, and TERS experiments were performed using the Bruker IRIS and a custom-written LabView software. After TERS imaging, the probe was lifted 200 µm away from the sample surface, and confocal Raman imaging was performed using the same conditions as in TERS imaging. Confocal Raman and TERS spectra were recorded using a confocal pinhole of 65 µm. Recording of a single AFM image took *ca.* 4 minutes, while *ca.* 8 minutes were needed for measuring either confocal Raman or TERS images. To ensure that the TERS imaging conditions (e.g., laser intensity or imaging force) did not damage the sample, AFM imaging of the analyzed PS-PMMA blend region was performed after the experiment. However, no mechanical or thermal damage of the sample was observed, as shown in Figure S2.

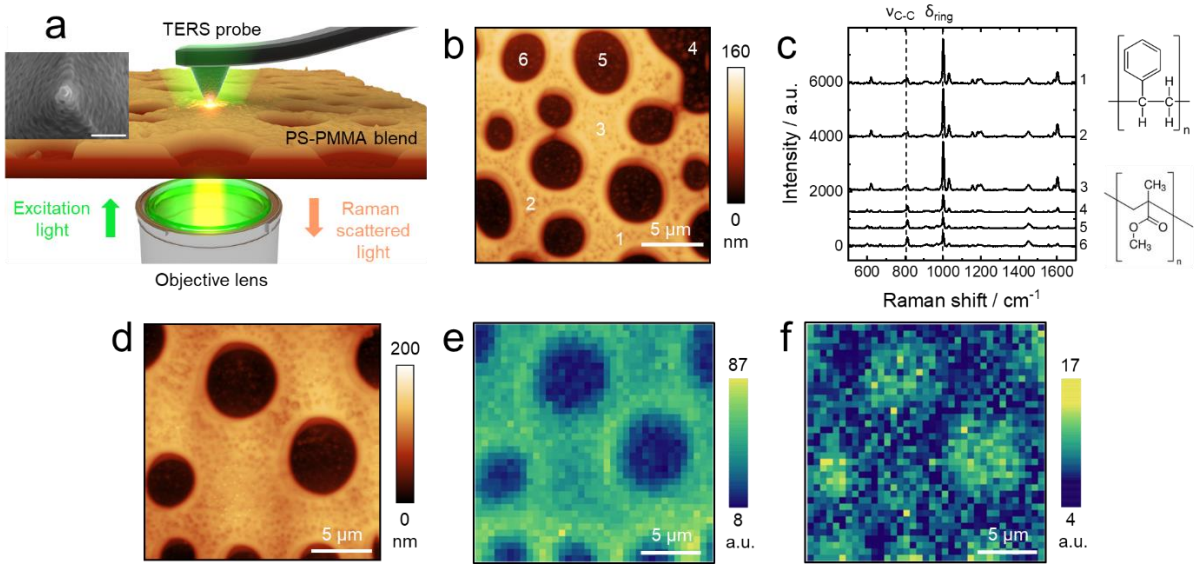

Figure 1. (a) Scheme of the transmission-mode AFM-TERS setup used for AFM, confocal Raman and TERS measurements in this study. Inset displays a scanning electron microscopy image of a representative Ag-coated TERS probe. Inset scale bar: 300 nm. (b) AFM topography image of a PS-PMMA blend. (c) Confocal Raman spectra measured at the locations marked in (b). Chemical structures of PS and PMMA are shown in the inset. Integration time: 30 s. PS and PMMA Raman marker bands at 1001 cm^{-1} and 813 cm^{-1}, respectively, are highlighted with dashed lines. (d) AFM topography image of the PS-PMMA blend. Correlative confocal Raman images of PS-PMMA blend constructed using intensity of (e) PS and (f) PMMA marker bands, respectively. Spectrum integration time: 1 s.

TERS probe preparation. TERS probes were prepared by coating AFM cantilevers (HQ:NSC14/No Al) with Ag (temper-annealed Ag wire, 99.99% purity, Advent Research Materials, UK) using thermal evaporation. The surface of Si AFM cantilevers was first oxidized to *ca.* 300 nm of SiO_2 in a furnace (Carbolite Gero, UK) at 1000 °C for 23 h to decrease their

surface refractive index.[45] Next, the probes were treated in a UV/Ozone cleaner (Ossila, UK) for 1 h. Finally, oxidized Si cantilevers were coated with a 100-nm thick layer of Ag at a deposition rate of 0.05 nm/s and a pressure of ~10^{-7} mbar. A scanning electron microscopy image of a representative TERS probe is presented in the inset of Figure 1a. The thermal evaporation system was housed inside a nitrogen glovebox (MB200B EcoVAP, MBraun, Germany) with O_2 and H_2O concentrations of <0.1 ppm to prevent contamination and preserve the plasmonic activity of TERS probes.

XPS measurements. A sigma II instrument (Thermo Scientific) equipped with an Alpha 110 hemispherical analyzer was used for XPS measurements. The instrument was operated in the large-area mode using a Mg Kα source at 100 W. XPS spectra were recorded at a takeoff angle of 90° and a source-to-input angle of 55°. The chamber pressure was maintained below 10^{-8} mbar during all measurements. A pass energy of 50 eV, an energy step size of 1 eV, and a 50 ms dwell time were used in collecting the survey scans, while the pass energy and step size were reduced to 25 eV and 0.1 eV, respectively, for the narrow region scans. In the XPS spectra, the C1s peak was aligned at 285 eV to compensate for the sample charging.[46]

Data analysis. Gwyddion (version 2.59) was used for the AFM image analysis, whilst a custom-written Mathematica script and OriginPro 2021 (version 9.8.0.200) software were used for the analysis of confocal Raman and TERS data. AFM images were leveled and background-corrected. Raman spectra were baseline-corrected using the least asymmetric square method and the height of PS and PMMA Raman marker bands was used to construct confocal Raman and TERS images.

RESULTS AND DISCUSSION

PS-PMMA blends were first investigated using AFM imaging and confocal Raman spectroscopy. The AFM topography image of the PS-PMMA blend surface exhibits rounded depressions of up to 3 μm in diameter, located ~120 nm below the top surface (Figures 1b, S3a, and S3b). The PS-PMMA film thickness was estimated to be ~530 nm (Figure S3a and S3b). Large area AFM image presented in Figure S3c shows that the depressions have a variable size, which makes it difficult to estimate their surface area coverage. Confocal Raman spectra recorded at the top surface and inside the depressions are shown in Figure 1c. Individual bands in the blend spectrum were assigned by comparison with the Raman spectra of pristine polymers films, which are presented in Figure S4. Interestingly, the blend spectra showed only a single PMMA Raman band at 813 cm^{-1} (C-C stretching vibration, $\nu_{C\text{-}C}$),[47] and multiple PS bands. Unsurprisingly, more PS bands are visible in the blend spectrum because PS Raman cross-section is much higher than PMMA, which is evident from the spectra of pristine polymers recorded under identical conditions (Figure S4c). The most intense PS band at 1001 cm^{-1} (phenyl ring deformation, δ_{ring})[47] was used as the Raman marker for PS, while the band at 813 cm^{-1} was used as PMMA marker. In Figure 1c, relative intensity of 1001 cm^{-1} band is found to be much higher on the top surface, whilst the 813 cm^{-1} band showed a relatively higher intensity inside the depressions, indicating that the blend surface is rich in PS, whilst the depressions are PMMA-rich domains. Polymer blends can also be

characterized using AFM phase imaging.[48] AFM phase imaging of the PS-PMMA sample used in this study is presented in Figure S5. The phase image in Figure S5b displays a slight contrast at the boundary between PS and PMMA domains, which gives an impression of phase change between the two regions. However, a cross-section profile across a domain boundary in the vertical direction presented in Figure S5c shows no phase change between the PS and PMMA domains. Therefore, the phase image contrast is an artefact arising from interaction of the sample with an asymmetrical probe apex. As the probe scans in the horizontal direction, different sides of the probe apex interact with left and right sides of the PS-PMMA boundary making the left side of the boundary look darker and the right side brighter than the surrounding features. Moreover, the AFM phase signal also contains a contribution from the tip energy dissipation during tapping, which cannot be directly converted into variations of the sample nanomechanical properties.[49,50] Therefore, the AFM phase imaging may not be a reliable indicator of phase separation in samples exhibiting similar physical properties.

Correlative AFM and confocal Raman imaging of a PS-PMMA region was performed to further validate the phase separation in the blend. Figures 1d-1f display AFM topography and confocal Raman images, constructed using PS and PMMA Raman marker bands, of the same blend region. Notably, the PS Raman image (Figure 1e) matches the AFM topography image (Figure 1d) perfectly, confirming that the top surface is a PS-rich domain. On the other hand, a relatively higher 813 cm^{-1} signal is observed inside the depressions (Figure 1f), confirming that these are PMMA-rich domains. From now on, PS- and PMMA-rich regions will be simply referred to as PS and PMMA domains.

Prior to performing TERS imaging of the polymer blend, we checked the plasmonic enhancement of PS and PMMA Raman signals on pristine films in the TERS near-field. For this, the TERS probe was kept in contact with the PS and PMMA films, whilst the excitation laser was moved in a raster fashion using a piezo mirror to record Raman spectra around the probe apex, generating so-called "hotspot" images (Figure S6). Interestingly, whilst a significant plasmonic enhancement of the 1001 cm^{-1} band was observed on the PS film (Figures S6a and S6c), no plasmonic enhancement of the 813 cm^{-1} band was observed on the PMMA film (Figures S6b and S6d). Similar measurements performed on pristine polymer films using different TERS probes gave the same results. Next, we checked the plasmonic enhancement of Raman signals in the PS-PMMA blend. A hotspot image of a TERS probe apex placed on the blend surface is presented in Figure S7. Comparison of the Raman spectra recorded at the probe apex and 1 μm away from it shows a 3× higher intensity of the PS marker band in the apex vicinity, thus confirming a strong plasmonic enhancement of PS signal in the TERS near-field. We also checked the plasmonic enhancement of signals in the PS and PMMA domains of the polymer blend using the same TERS probe, which is shown in Figure S8. Whilst a similar plasmonic enhancement of PS signal was observed in the PS and PMMA domains, the PMMA band at 813 cm^{-1} was not enhanced most likely either due to the significantly lower Raman cross-section of PMMA compared to PS or due to the spatial arrangement of O-C=O moiety in PMMA molecules being orthogonal to the

polarization of TERS near-field. Therefore, analysis of the TERS data was performed using the PS signals.

Correlative AFM topography, confocal Raman, and TERS images of the PS-PMMA blend are shown in Figure 2. As expected, the topography image (Figure 2a) and confocal Raman image of the PS marker band intensity (Figure 2b) match very well, clearly distinguishing the PS and PMMA domains from each other. The confocal PS signal intensity recorded at 20 locations within the PS and PMMA domains is shown in Figure 2c. PS content was clearly higher in the PS domain

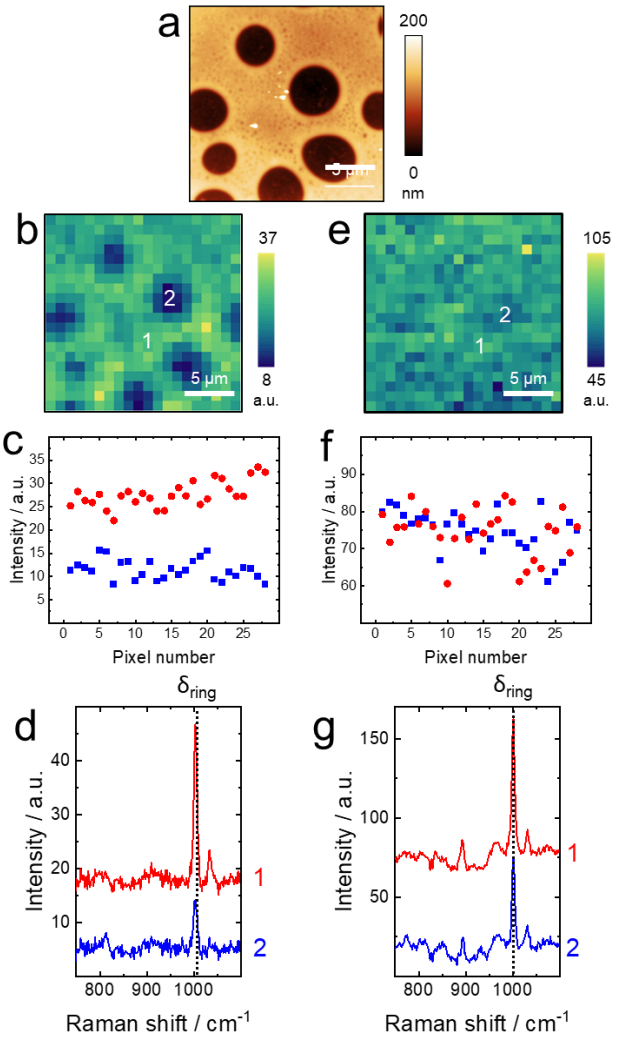

Figure 2. (a) AFM topography image and (b) confocal Raman image of the PS signal intensity measured in the same region of PS-PMMA blend. Spectrum integration time: 1 s. (c) PS Raman signal intensity recorded at 20 different positions within PS (red) and PMMA (blue) domains identified in (b). (d) Average of 9 confocal Raman spectra measured at the positions marked in the PS and PMMA domains in (b). (e) TERS image of PS signal intensity measured in the same region of blend shown in (a). Spectrum integration time: 1 s. (f) Plot of PS TERS signal intensity recorded at 20 different positions at the location of PS (red) and PMMA (blue) domains labelled in (e). (g) Average of 9 TERS spectra measured at the positions marked in (e).

than in the PMMA domain. Averaged confocal Raman spectra measured in PS and PMMA domains show that the PS signal is 92% lower in the PMMA domain than in the PS domain (Figure 2d), indicating a significant lateral phase-separation.

Surprisingly, a TERS image of the same sample region (Figure 2e) showed barely any difference in the PS signal intensity between the PS and PMMA domains compared to the confocal Raman image (Figure 2b). The PS signal intensity recorded at 20 different positions within the PS and PMMA domains using TERS is plotted in Figure 2f. Interestingly, no noticeable difference in the PS signal intensity is observed between the PS and PMMA domains. Furthermore, the averaged TERS spectra (Figure 2g) measured at the positions marked in Figure 2e show that PS intensity difference between the PS and PMMA domains is only 13%. The reproducibility of these results was confirmed by performing similar measurements and analysis in another region of the PS-PMMA blend, which are presented in Figure S9.

Since the TERS signal is the sum of the near-field signal generated at the TERS probe apex and the confocal Raman signal, TERS images (Figures 2e and S9e) often show some resemblance to their confocal Raman image counterparts (Figures 2b and S9b). However, the contrast between the PS and PMMA domains in the TERS and confocal Raman images is completely different. Whilst the confocal Raman image suggests that PS and PMMA are laterally phase-separate into different domains, the TERS image suggests that there is very little, if any lateral phase separation at all.

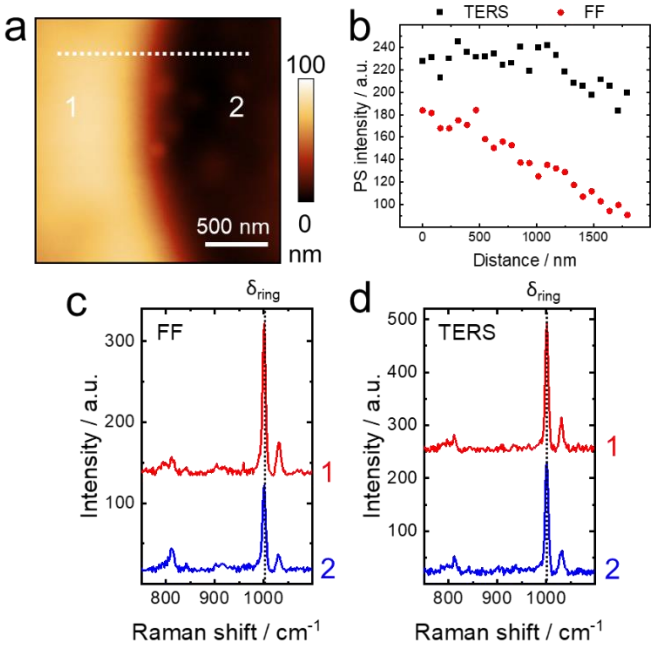

Figure 3. (a) AFM topography image of a domain boundary in PS-PMMA blend. (b) Plots of confocal Raman (CR) and TERS PS signal intensity measured along the line (left to right) marked in (a). Step size: 78 nm. Averaged (c) CR and (d) TERS spectra measured in the PS and PMMA domains at the positions marked in (a). Spectrum integration time: 10 s.

To probe deeper into this, we performed further analysis of a boundary between the PS and PMMA domains using a longer acquisition time (10 s) to obtain higher signal-to-noise ratio

spectra. An AFM topography image of the PS-PMMA boundary region is shown in Figure 3a. The confocal Raman and TERS PS signal intensity measured along the line marked in Figure 3a with a step size of 78 nm is plotted in Figure 3b. As expected, the confocal Raman PS signal decreases linearly whilst going from the PS to the PMMA domain. In contrast, the TERS PS signal intensity shows only a very slight change. To look at it more quantitatively, an average of 5 confocal Raman spectra recorded inside the PMMA and PS domains (marked as positions 1 and 2 in Figure 3a) are plotted in Figure 3c. The PS signal intensity is found to be 47% lower in the PMMA compared to the PS domain. Conversely, in the averaged TERS spectra measured at the same locations (Figure 3d), only a 12% decrease in PS signal intensity was observed. Once again, confocal Raman results indicate a clear lateral phase separation of the blend into PS and PMMA domains, whereas the TERS measurements point towards the opposite trend of little or no phase separation. Figure S10 shows similar results obtained at another PS-PMMA domain boundary, validating the reproducibility of these results.

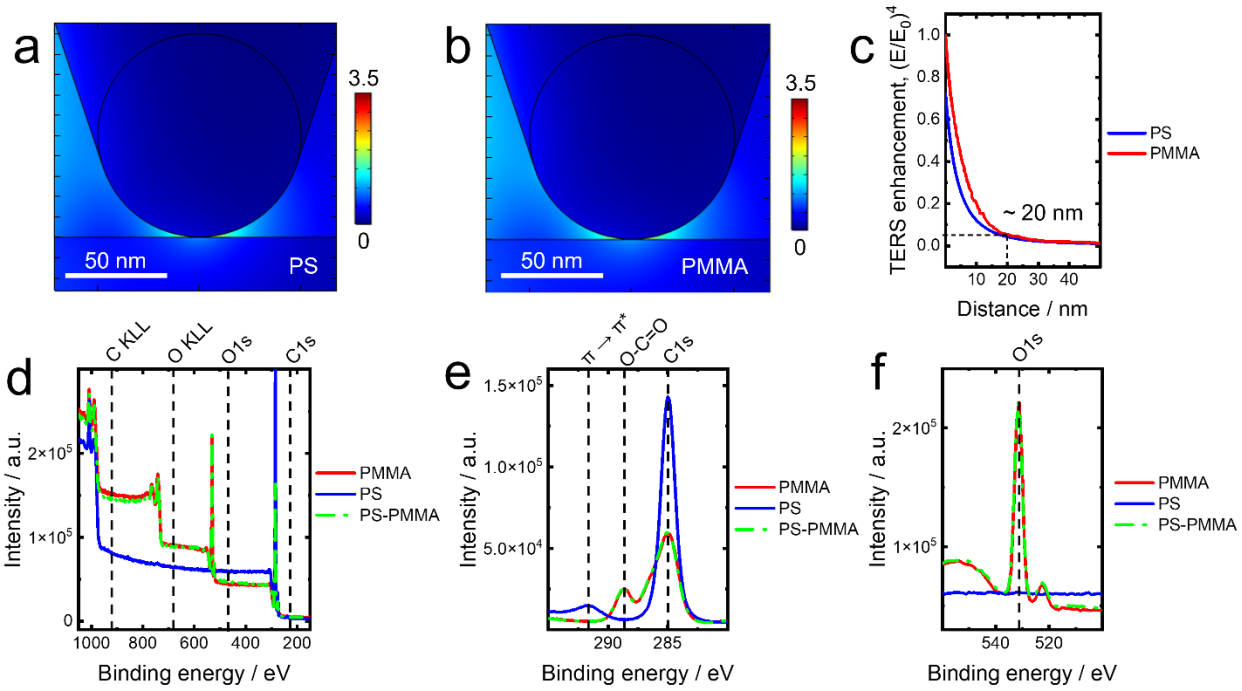

Figure 4. Simulated electric field enhancement (E/E_0) image of a Ag probe in contact with (a) PS and (b) PMMA surface under 532 nm laser illumination. (c) TERS signal enhancement $(E/E_0)^4$ as a function of distance within the polymer sample. (d) XPS survey spectra of PS (blue), PMMA (red) and PS-PMMA blend (green) samples. High-resolution (e) O1s and (f) C1s XPS spectra of PS (blue), PMMA (red) and PS-PMMA blend (green).

To understand the discrepancy between the confocal Raman and TERS results, we need to consider the different sampling volumes of the two techniques. The TERS information depth (defined as the depth where 95% of the signal comes from) was calculated using numerical simulations of the electric field enhancement at a TERS probe apex mimicking the experimental conditions employed in our TERS measurements (see Supplementary Note 1 for details). The simulated electric field enhancement (E/E_0) image of a Ag probe in contact with PS and PMMA surface is presented in Figures 4a and 4b, respectively. From the plot of the TERS signal enhancement $(E/E_0)^4$ as a function of distance from the probe apex (Figure 4c), the TERS information depth inside PS and PMMA surfaces is calculated to be 18 and 20 nm, respectively.

On the other hand, axial resolution (R_{Axial}) of a confocal Raman microscope is defined as[51,52]

$$R_{Axial} = \frac{1.4\lambda n}{NA^2} \quad (1)$$

where, λ is the excitation laser wavelength, n is the refractive index of the medium and NA is the numerical aperture of the objective lens. Using Equation 1, the depth resolution of confocal Raman measurements in PS and PMMA films is calculated to be 533 nm and 500 nm, respectively. Considering the average thickness of PS-PMMA blend, which is *ca.* 630 nm, this means that confocal Raman measurements probe the bulk of the film, thus providing ensemble information. Therefore, whilst confocal Raman imaging and spectroscopy results in Figures 1-3, S9 and S10 indicate a lateral phase separation into distinct PS and PMMA domains in the bulk, the surface sensitivity of TERS measurements (Figures 2, 3, S9 and S10) indicates the presence of a uniform PS film in the top 20 nm of the entire blend surface.

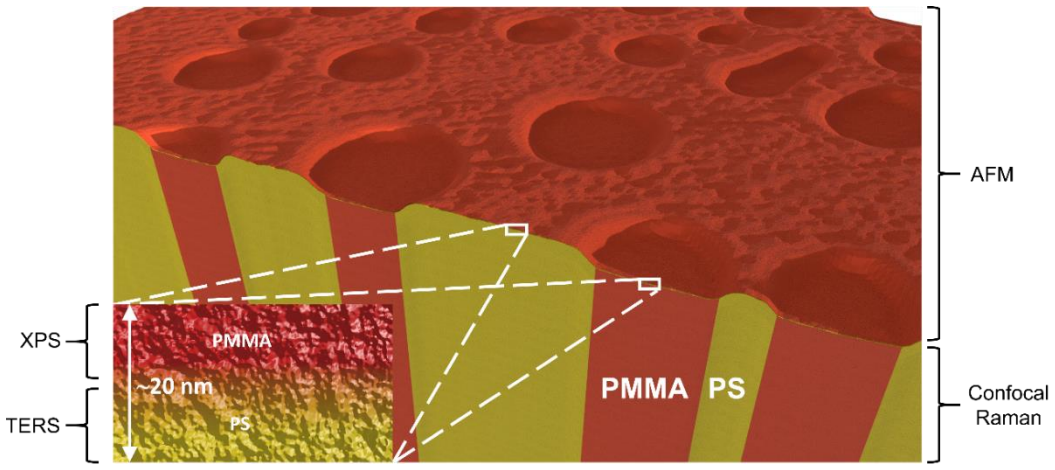

Figure 5. Schematic illustration of the proposed PS-PMMA blend structure based on the correlative AFM, confocal Raman, TERS and XPS measurements. Laterally phase-separated PS and PMMA domains revealed by AFM and confocal Raman imaging are covered with a continuous surface layer of vertically phase-separated PMMA and PS revealed by XPS and TERS, as shown in the inset.

Finally, to verify the surface chemical composition of the blend, we performed XPS measurements on pristine PS and PMMA and PS-PMMA blends films. Figures 4d-f display survey, C1s, and O1s XPS spectra of PS, PMMA, and PS-PMMA blend films, respectively. Interestingly, spectral features of all three XPS spectra of the PS-PMMA blend film perfectly match those of PMMA spectra. For example, whilst no oxygen signal was detected on the PS film surface, the level of oxygen content detected on the blend and PMMA surfaces was exactly the same (Figure 4d and 4f). Similarly, in the high resolution C1s spectra, O-C=O signal (indictive of the PMMA structure) in the PS-PMMA surface matched perfectly with the PMMA film as shown in Figure 4e. The information depth of XPS in the PS-PMMA blend, where 95% of the signal was obtained, was calculated to be 9.2 nm as described in the Supplementary Note 2.

The XPS results thus confirm that the PS-PMMA blend surface is covered with a PMMA layer of at least 9.2 nm thickness. However, if only PMMA was present on the surface, the PS signal would not be plasmonically enhanced in the TERS near-field. In other words, the difference in PS signal intensity between the PS and PMMA domains in TERS would have been similar to that observed in confocal Raman spectroscopy. On the contrary, TERS showed a similar plasmonic enhancement of PS signal in both PS and PMMA domains (Figure S8). Furthermore, the PS signal intensity was found to be nearly constant in the PS and PMMA domains (Figures 2, 3, S9 and S10), indicating that within the TERS information depth of 20 nm, a uniform PS layer was present over the entire blend surface. This shows that in the non-gap mode TERS measurements of these polymer samples, the sampling depth of TERS near-field is a few tens of nanometers. Considering that XPS sampling depth was significantly lower than that of TERS, it is evident that PS and PMMA are vertically phase-separated within 20 nm of the blend surface with PMMA present at the top. A schematic depiction of the proposed PS-PMMA blend structure based on the correlative AFM, confocal Raman, TERS, and XPS measurements is presented in Figure 5. Note that whilst the four individual techniques provide valuable information, none of them can fully describe the polymer blend structure alone. The full picture is revealed only by correlating the complementary structural, molecular, and elemental information.

We want to highlight that not all techniques with nanoscale resolution can always provide clear information about polymer blend phase separation. For example, we also performed correlative scanning transmission electron microscopy (STEM) and energy dispersive spectroscopy (EDS) imaging of the PS-PMMA blend cross-section by cutting the sample with FIB milling (using focused Ga ions). While some contrast was observed at the PS-PMMA surface in the STEM images, it did not correlate with the EDS image of O signal. Therefore, the vertical phase separation at the blend surface was not entirely clear. It could be due to sample alteration/damage during FIB milling since focused Ga ions have a different etching rate towards PS and PMMA. It is possible that one polymer was selectively removed from the sample altering the polymer blend structure.

Notably, mechanism of PS-PMMA film formation during spin coating was investigated by Heriot and Jones.[11] In the initial stage of spin-coating, the wetting polymer layers were found to phase separate vertically. In the later stage, the polymer film destabilized due to solvent

evaporation and polymers rearranged with a lateral phase separation in bulk. In line with these findings, our confocal Raman measurements also demonstrated the lateral phase separation of PS and PMMA in bulk. However, the diffraction-limited spatial resolution of the light scattering techniques used by Heriot and Jones precluded observation of the nanoscale vertical phase, which was revealed using XPS and TERS measurements in our study.

CONCLUSIONS

In summary, we have performed a comprehensive investigation of phase separation in PS-PMMA polymer blends at the nanoscale using a complementary set of analytical tools that include AFM, confocal Raman spectroscopy, TERS, and XPS. The results presented herein clearly indicate that PS-PMMA blend components were not only phase-separated into distinct PS and PMMA domains laterally in the bulk, but also vertically at the surface, as illustrated in Figure 5. Whilst AFM, XPS, and confocal Raman spectroscopy have been used for characterization of polymer blends before, this is the first time that a clear vertical phase separation within 20 nm of the PS-PMMA blend surface was revealed, due to the TERS surface sensitivity. This work demonstrates that correlation of complementary topographical, molecular, and elemental information provides a complete picture of the lateral and vertical phase separation in this important class of polymer materials, which cannot be determined by any single technique alone. We believe that our methodology can also be used to study phase separation in thick block copolymer samples by cutting them into thin sections. Given the demonstrated unique ability of TERS to probe surface phase separation, we envisage that it can become an important complementary analytical tool for nanoscale polymer characterization and contribute significantly to the advancement of polymer-based technologies.

ASSOCIATED CONTENT

Supporting Information. Additional AFM, confocal Raman, and TERS measurements to demonstrate reproducibility of experimental results and stability of our AFM-based TERS setup. Details of numerical simulations and TERS information depth calculations. Details of XPS information depth calculation.

AUTHOR INFORMATION

Corresponding Authors

Naresh Kumar - Department of Chemistry and Applied Biosciences, ETH Zurich, CH-8093 Zurich, Switzerland. kumar@org.chem.ethz.ch

Renato Zenobi - Department of Chemistry and Applied Biosciences, ETH Zurich, CH-8093 Zurich, Switzerland. zenobi@org.chem.ethz.ch

Author Contributions

The manuscript was written through contributions of all authors. All authors have given approval to the final version of the manuscript.

ACKNOWLEDGMENT

The authors thank Dr. Alex G. Shard from the National Physical Laboratory, UK for useful discussion of the XPS information depth, the ScopeM facility at ETH Zurich for access to the SEM instrumentation and Christian Marro and Christoph André Bärtschi from the ETH mechanical workshop for help with the experimental setup. D.M., N.K, and R.Z. acknowledge financial support from the European Union through ERC grant no. 741431 (2D Nano-Spec).

REFERENCES

(1) Li, X.; Gao, J.; Xue, L.; Han, Y. Porous Polymer Films with Gradient-Refractive-Index Structure for Broadband and Omnidirectional Antireflection Coatings. *Adv. Funct. Mater.* **2010**, *20* (2), 259–265. https://doi.org/10.1002/adfm.200901052.

(2) Segalman, R. A. Patterning with Block Copolymer Thin Films. *Mater. Sci. Eng. R Reports* **2005**, *48* (6), 191–226. https://doi.org/10.1016/j.mser.2004.12.003.

(3) Halls, J. J. M.; Walsh, C. A.; Greenham, N. C.; Marseglia, E. A.; Friend, R. H.; Moratti, S. C.; Holmes, A. B. Efficient Photodiodes from Interpenetrating Polymer Networks. *Nature* **1995**, *376* (6540), 498–500. https://doi.org/10.1038/376498a0.

(4) Moons, E. Conjugated Polymer Blends: Linking Film Morphology to Performance of Light Emitting Diodes and Photodiodes. *J. Phys. Condens. Matter* **2002**, *14* (47), 12235–12260. https://doi.org/10.1088/0953-8984/14/47/301.

(5) Budkowski, A.; Zemła, J.; Moons, E.; Awsiuk, K.; Rysz, J.; Bernasik, A.; Björström-Svanström, C. M.; Lekka, M.; Jaczewska, J. Polymer Blends Spin-Cast into Films with Complementary Elements for Electronics and Biotechnology. *J. Appl. Polym. Sci.* **2012**, *125* (6), 4275–4284. https://doi.org/10.1002/app.36574.

(6) Hester, J. F.; Banerjee, P.; Mayes, A. M. Preparation of Protein-Resistant Surfaces on Poly(Vinylidene Fluoride) Membranes via Surface Segregation. *Macromolecules* **1999**, *32* (5), 1643–1650. https://doi.org/10.1021/ma980707u.

(7) Ton-That, C.; Shard, A. G.; Daley, R.; Bradley, R. H. Effects of Annealing on The5 Surface Composition and Morphology of PS/PMMA Blend. *Macromolecules* **2000**, *33* (22), 8453–8459. https://doi.org/10.1021/ma000792h.

(8) Tanaka, K.; Yoon, J. S.; Takahara, A.; Kajiyama, T.; Yoon, J. S. Ultrathinning-Induced Surface Phase Separation of Polystyrene/Poly(Vinyl Methyl Ether) Blend Film. *Macromolecules* **1995**, *28* (4), 934–938. https://doi.org/10.1021/ma00108a021.

(9) Schmidt, J. J.; Gardella, J. A.; Salvati, L. Surface Studies of Polymer Blends. 2. An ESCA and IR Study of Poly(Methyl Methacrylate)/Poly(Vinyl Chloride) Homopolymer Blends.

Macromolecules **1989**, *22* (12), 4489–4495. https://doi.org/10.1021/ma00202a019.

(10) Walheim, S.; Böltau, M.; Mlynek, J.; Krausch, G.; Steiner, U. Structure Formation via Polymer Demixing in Spin-Cast Films. *Macromolecules* **1997**, *30* (17), 4995–5003. https://doi.org/10.1021/ma9619288.

(11) Heriot, S. Y.; Jones, R. A. L. An Interfacial Instability in a Transient Wetting Layer Leads to Lateral Phase Separation in Thin Spin-Cast Polymer-Blend Films. *Nat. Mater.* **2005**, *4* (10), 782–786. https://doi.org/10.1038/nmat1476.

(12) Li, H.; Cooper-White, J. J. Changing Ligand Number and Type within Nanocylindrical Domains through Kinetically Constrained Self-Assembly-Impacts of Ligand "redundancy" on Human Mesenchymal Stem Cell Adhesion and Morphology. *Biomater. Sci.* **2014**, *2* (11), 1693–1705. https://doi.org/10.1039/c4bm00109e.

(13) Riaz, U.; Ashraf, S. M. Characterization of Polymer Blends with FTIR Spectroscopy. *Charact. Polym. Blends Miscibility, Morphol. Interfaces* **2015**, *9783527331*, 625–678. https://doi.org/10.1002/9783527645602.ch20.

(14) Huan, S.; Lin, W.; Sato, H.; Yang, H.; Jiang, J.; Ozaki, Y.; Wu, H.; Shen, G.; Yu, R. Direct Characterization of Phase Behavior and Compatibility in PET/HDPE Polymer Blends by Confocal Raman Mapping. *J. Raman Spectrosc.* **2007**, *38* (3), 260–270. https://doi.org/10.1002/jrs.1636.

(15) Bonnin, E. A.; Rizzoli, S. O. Novel Secondary Ion Mass Spectrometry Methods for the Examination of Metabolic Effects at the Cellular and Subcellular Levels. *Front. Behav. Neurosci.* **2020**, *14* (July), 1–13. https://doi.org/10.3389/fnbeh.2020.00124.

(16) Kurouski, D.; Dazzi, A.; Zenobi, R.; Centrone, A. Infrared and Raman Chemical Imaging and Spectroscopy at the Nanoscale. *Chem. Soc. Rev.* **2020**, *49* (11), 3315–3347. https://doi.org/10.1039/C8CS00916C.

(17) Uemura, T.; Kaseda, T.; Sasaki, Y.; Inukai, M.; Toriyama, T.; Takahara, A.; Jinnai, H.; Kitagawa, S. Mixing of Immiscible Polymers Using Nanoporous Coordination Templates. *Nat. Commun.* **2015**, *6* (1), 7473. https://doi.org/10.1038/ncomms8473.

(18) Wang, L.; Liu, D.; Zhang, F.; Zhang, Z.; Cui, J.; Jia, Z.; Yu, Z.; Lv, Y.; Liu, W. Dynamics of the Charging-Induced Imaging Instability in Transmission Electron Microscopy. *Nanoscale Adv.* **2021**, *3* (11), 3035–3040. https://doi.org/10.1039/d1na00140j.

(19) Kuei, B.; Gomez, E. D. Pushing the Limits of High-Resolution Polymer Microscopy Using Antioxidants. *Nat. Commun.* **2021**, *12* (1), 153. https://doi.org/10.1038/s41467-020-20363-1.

(20) Kumar, N.; Mignuzzi, S.; Su, W.; Roy, D. Tip-Enhanced Raman Spectroscopy: Principles and Applications. *EPJ Tech. Instrum.* **2015**, *2* (1), 9. https://doi.org/10.1140/epjti/s40485-015-0019-5.

(21) Kumar, N.; Weckhuysen, B. M.; Wain, A. J.; Pollard, A. J. Nanoscale Chemical Imaging Using Tip-Enhanced Raman Spectroscopy. *Nat. Protoc.* **2019**, *14* (4), 1169–1193.

https://doi.org/10.1038/s41596-019-0132-z.

(22) Brown, R. J. C.; Milton, M. J. T. Nanostructures and Nanostructured Substrates for Surface-Enhanced Raman Scattering (SERS). *J. Raman Spectrosc.* **2008**, *39* (10), 1313–1326. https://doi.org/10.1002/jrs.2030.

(23) Kleinman, S. L.; Frontiera, R. R.; Henry, A. I.; Dieringer, J. A.; Van Duyne, R. P. Creating, Characterizing, and Controlling Chemistry with SERS Hot Spots. *Phys. Chem. Chem. Phys.* **2013**, *15* (1), 21–36. https://doi.org/10.1039/c2cp42598j.

(24) Sharma, B.; Frontiera, R. R.; Henry, A. I.; Ringe, E.; Van Duyne, R. P. SERS: Materials, Applications, and the Future. *Mater. Today* **2012**, *15* (1–2), 16–25. https://doi.org/10.1016/S1369-7021(12)70017-2.

(25) Su, W.; Kumar, N.; Mignuzzi, S.; Crain, J.; Roy, D. Nanoscale Mapping of Excitonic Processes in Single-Layer MoS 2 Using Tip-Enhanced Photoluminescence Microscopy. *Nanoscale* **2016**, *8* (20), 10564–10569. https://doi.org/10.1039/C5NR07378B.

(26) Su, W.; Kumar, N.; Krayev, A.; Chaigneau, M. In Situ Topographical Chemical and Electrical Imaging of Carboxyl Graphene Oxide at the Nanoscale. *Nat. Commun.* **2018**, *9* (1), 2891. https://doi.org/10.1038/s41467-018-05307-0.

(27) Su, W.; Esfandiar, A.; Lancry, O.; Shao, J.; Kumar, N.; Chaigneau, M. Visualising Structural Modification of Patterned Graphene Nanoribbons Using Tip-Enhanced Raman Spectroscopy. *Chem. Commun.* **2021**, *57* (56), 6895–6898. https://doi.org/10.1039/D1CC01769A.

(28) Su, W.; Kumar, N.; Shu, H.; Lancry, O.; Chaigneau, M. In Situ Visualization of Optoelectronic Behavior of Grain Boundaries in Monolayer WSe 2 at the Nanoscale. *J. Phys. Chem. C* **2021**, *125* (48), 26883–26891. https://doi.org/10.1021/acs.jpcc.1c08064.

(29) Kumar, N.; Marchesini, S.; Howe, T.; Edwards, L.; Brennan, B.; Pollard, A. J. Nanoscale Characterization of Plasma Functionalized Graphitic Flakes Using Tip-Enhanced Raman Spectroscopy. *J. Chem. Phys.* **2020**, *153* (18), 184708. https://doi.org/10.1063/5.0024370.

(30) Kumar, N.; Stephanidis, B.; Zenobi, R.; Wain, A. J.; Roy, D. Nanoscale Mapping of Catalytic Activity Using Tip-Enhanced Raman Spectroscopy. *Nanoscale* **2015**, *7* (16), 7133–7137. https://doi.org/10.1039/C4NR07441F.

(31) Kumar, N.; Wondergem, C. S.; Wain, A. J.; Weckhuysen, B. M. In Situ Nanoscale Investigation of Catalytic Reactions in the Liquid Phase Using Zirconia-Protected Tip-Enhanced Raman Spectroscopy Probes. *J. Phys. Chem. Lett.* **2019**, *10* (8), 1669–1675. https://doi.org/10.1021/acs.jpclett.8b02496.

(32) Cai, Z. F.; Merino, J. P.; Fang, W.; Kumar, N.; Richardson, J. O.; De Feyter, S.; Zenobi, R. Molecular-Level Insights on Reactive Arrangement in On-Surface Photocatalytic Coupling Reactions Using Tip-Enhanced Raman Spectroscopy. *J. Am. Chem. Soc.* **2022**, *144* (1), 538–546. https://doi.org/10.1021/jacs.1c11263.

(33) Kumar, N.; Kalirai, S.; Wain, A. J.; Weckhuysen, B. M. Nanoscale Chemical Imaging of a

Single Catalyst Particle with Tip-Enhanced Fluorescence Microscopy. *ChemCatChem* **2019**, *11* (1), 417–423. https://doi.org/10.1002/cctc.201801023.

(34) Kumar, N.; Zoladek-Lemanczyk, A.; Guilbert, A. A. Y.; Su, W.; Tuladhar, S. M.; Kirchartz, T.; Schroeder, B. C.; McCulloch, I.; Nelson, J.; Roy, D.; Castro, F. A. Simultaneous Topographical, Electrical and Optical Microscopy of Optoelectronic Devices at the Nanoscale. *Nanoscale* **2017**, *9* (8), 2723–2731. https://doi.org/10.1039/C6NR09057E.

(35) Pandey, Y.; Kumar, N.; Goubert, G.; Zenobi, R. Nanoscale Chemical Imaging of Supported Lipid Monolayers Using Tip-Enhanced Raman Spectroscopy. *Angew. Chemie* **2021**, *133* (35), 19189–19194. https://doi.org/10.1002/ange.202106128.

(36) Kumar, N.; Drozdz, M. M.; Jiang, H.; Santos, D. M.; Vaux, D. J. Nanoscale Mapping of Newly-Synthesised Phospholipid Molecules in a Biological Cell Using Tip-Enhanced Raman Spectroscopy. *Chem. Commun.* **2017**, *53* (16), 2451–2454. https://doi.org/10.1039/C6CC10226C.

(37) Yeo, B.-S.; Amstad, E.; Schmid, T.; Stadler, J.; Zenobi, R. Nanoscale Probing of a Polymer-Blend Thin Film with Tip-Enhanced Raman Spectroscopy. *Small* **2009**, *5* (8), 952–960. https://doi.org/10.1002/smll.200801101.

(38) Xue, L.; Li, W.; Hoffmann, G. G.; Goossens, J. G. P.; Loos, J.; de With, G. High-Resolution Chemical Identification of Polymer Blend Thin Films Using Tip-Enhanced Raman Mapping. *Macromolecules* **2011**, *44* (8), 2852–2858. https://doi.org/10.1021/ma101651r.

(39) Harirchian-Saei, S.; Wang, M. C. P.; Gates, B. D.; Moffitt, M. G. Directed Polystyrene/Poly(Methyl Methacrylate) Phase Separation and Nanoparticle Ordering on Transparent Chemically Patterned Substrates. *Langmuir* **2012**, *28* (29), 10838–10848. https://doi.org/10.1021/la301298p.

(40) Harris, M.; Appel, G.; Ade, H. Surface Morphology of Annealed Polystyrene and Poly(Methyl Methacrylate) Thin Film Blends and Bilayers. *Macromolecules* **2003**, *36* (9), 3307–3314. https://doi.org/10.1021/ma0257043.

(41) Wang, C. W.; Moffitt, M. G. Use of Block Copolymer-Stabilized Cadmium Sulfide Quantum Dots as Novel Tracers for Laser Scanning Confocal Fluorescence Imaging of Blend Morphology in Polystyrene/Poly(Methyl Methacrylate) Films. *Langmuir* **2005**, *21* (6), 2465–2473. https://doi.org/10.1021/la047882q.

(42) Zong, Q.; Li, Z.; Xie, X. Inversion of Phase Morphology in Polymer-Blend Thin Films on Glass Substrates. *Macromol. Chem. Phys.* **2004**, *205* (8), 1116–1124. https://doi.org/10.1002/macp.200300235.

(43) Ahn, D. U.; Wang, Z.; Campbell, I. P.; Stoykovich, M. P.; Ding, Y. Morphological Evolution of Thin PS/PMMA Films: Effects of Surface Energy and Blend Composition. *Polymer (Guildf).* **2012**, *53* (19), 4187–4194. https://doi.org/10.1016/j.polymer.2012.07.037.

(44) Das, A.; Dey, A. B.; Chattopadhyay, S.; De, G.; Sanyal, M. K.; Mukherjee, R. Nanoparticle

Induced Morphology Modulation in Spin Coated PS/PMMA Blend Thin Films. *Langmuir* **2020**, *36* (50), 15270–15282. https://doi.org/10.1021/acs.langmuir.0c02584.

(45) Yeo, B. S.; Schmid, T.; Zhang, W.; Zenobi, R. Towards Rapid Nanoscale Chemical Analysis Using Tip-Enhanced Raman Spectroscopy with Ag-Coated Dielectric Tips. *Anal. Bioanal. Chem.* **2007**, *387* (8), 2655–2662. https://doi.org/10.1007/s00216-007-1165-7.

(46) Burrell, M. C.; Chera, J. J. Charge Correction of the Binding Energy Scale in XPS Analysis of Polymers Using Surface Deposition of PDMS. *Surf. Interface Anal.* **1999**, *27* (9), 811–815. https://doi.org/10.1002/(SICI)1096-9918(199909)27:9<811::AID-SIA636>3.0.CO;2-W.

(47) Matsushita, A.; Ren, Y.; Matsukawa, K.; Inoue, H.; Minami, Y.; Noda, I.; Ozaki, Y. Two-Dimensional Fourier-Transform Raman and near-Infrared Correlation Spectroscopy Studies of Poly(Methyl Methacrylate) Blends. 1. Immiscible Blends of Poly(Methyl Methacrylate) and Atactic Polystyrene. *Vib. Spectrosc.* **2000**, *24* (2), 171–180. https://doi.org/10.1016/S0924-2031(00)00062-X.

(48) Raghavan, D.; Gu, X.; Nguyen, T.; VanLandingham, M.; Karim, A. Mapping Polymer Heterogeneity Using Atomic Force Microscopy Phase Imaging and Nanoscale Indentation. *Macromolecules* **2000**, *33* (7), 2573–2583. https://doi.org/10.1021/ma991206r.

(49) Schön, P.; Bagdi, K.; Molnár, K.; Markus, P.; Pukánszky, B.; Julius Vancso, G. Quantitative Mapping of Elastic Moduli at the Nanoscale in Phase Separated Polyurethanes by AFM. *Eur. Polym. J.* **2011**, *47* (4), 692–698. https://doi.org/10.1016/j.eurpolymj.2010.09.029.

(50) García, R.; Tamayo, J.; San Paulo, A. Phase Contrast and Surface Energy Hysteresis in Tapping Mode Scanning Force Microscopy. *Surf. Interface Anal.* **1999**, *27* (5), 312–316. https://doi.org/10.1002/(SICI)1096-9918(199905/06)27:5/6<312::AID-SIA496>3.0.CO;2-Y.

(51) Juang, C.; Finzi, L.; Bustamante, C. J. Design and Application of a Computer-controlled Confocal Scanning Differential Polarization Microscope. *Rev. Sci. Instrum.* **1988**, *59* (11), 2399–2408. https://doi.org/10.1063/1.1139918.

(52) Webb, R. H. Confocal Optical Microscopy. *Reports Prog. Phys.* **1996**, *59* (3), 427–471. https://doi.org/10.1088/0034-4885/59/3/003.

Supporting Information

Visualizing Surface Phase Separation in PS-PMMA Polymer Blends at the Nanoscale

Dušan Mrđenović,[1] Daniel Abbott,[1] Victor Mougel,[1] Weitao Su,[2] Naresh Kumar,[1] and Renato Zenobi[1*]*

[1]Department of Chemistry and Applied Biosciences, ETH Zurich, CH-8093 Zurich, Switzerland

[2] College of Materials and Environmental Engineering, Hangzhou Dianzi University, 310018 Hangzhou, China

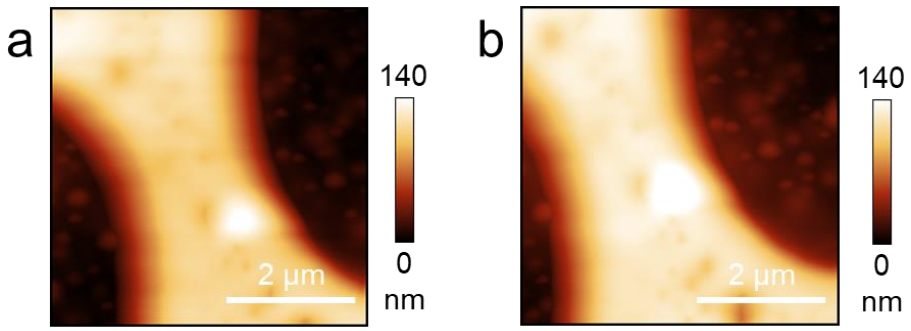

Figure S1. Time-series AFM topography image of a PS-PMMA blend recorded at (a) 0 and (b) 60 min.

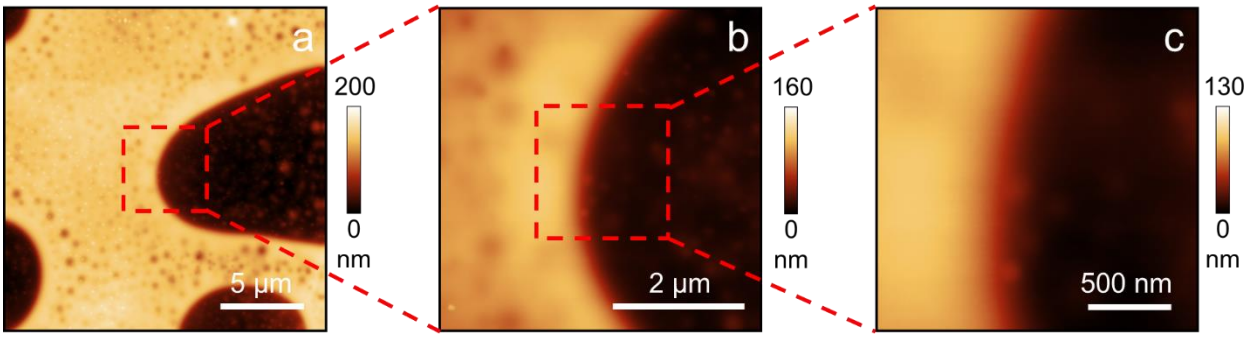

Figure S2. AFM topography images of (a) 20×20 µm^2, (b) 5×5 µm^2 and (c) 2×2 µm^2 areas of a PS-PMMA blend region recorded after confocal Raman and TERS measurements confirming no thermal or mechanical damage to the sample.

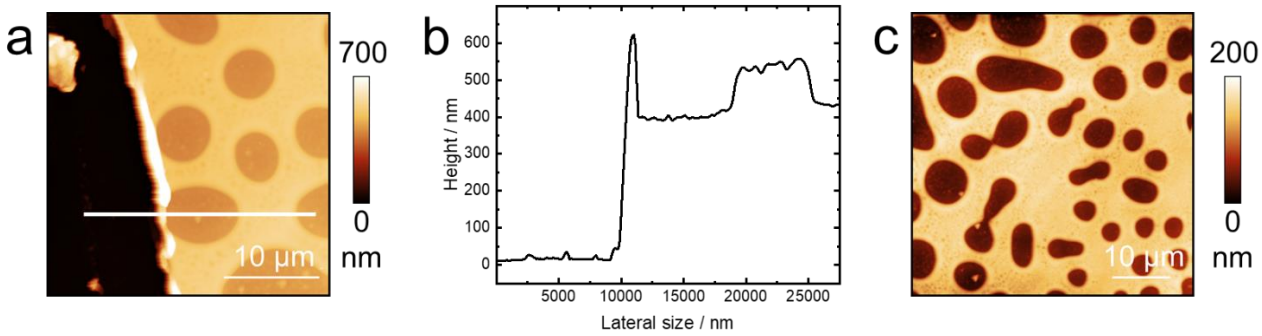

Figure S3. (a) AFM topography image a PS-PMMA blend and glass substrate. (b) The cross-sectional profile measured along the white line in Panel a. (c) AFM topography image a large PS-PMMA blend region.

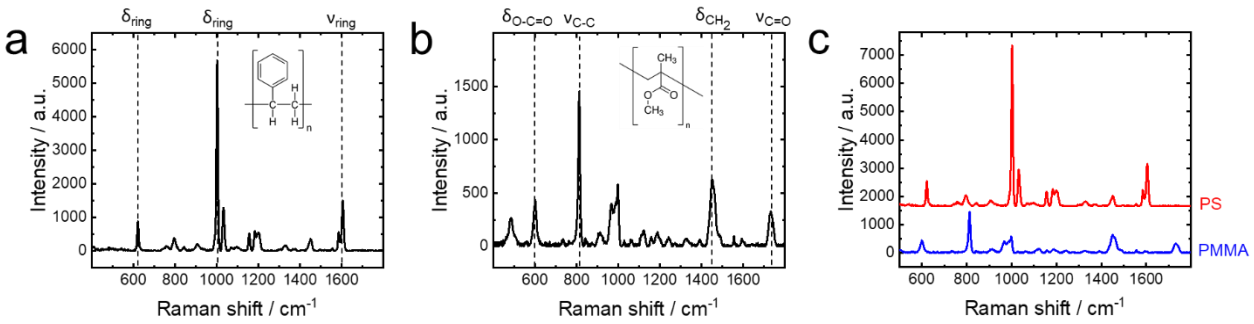

Figure S4. Confocal Raman spectra of (a) PS and (b) PMMA. Chemical structures of PS and PMMA are shown as insets. (c) PS and PMMA confocal Raman spectra plotted next to each other for easier Raman cross-section comparison. Integration time: 60 s. Prominent PS and PMMA Raman bands are assigned. δ – deformation, ν – stretching.

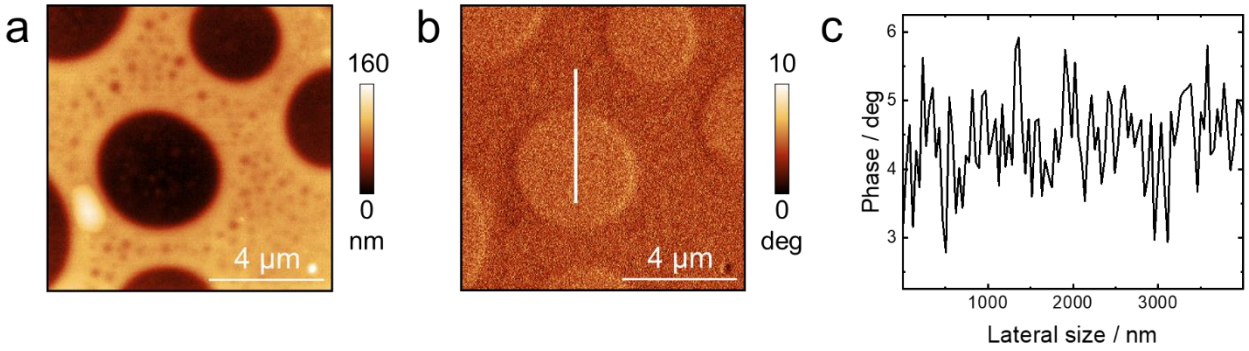

Figure S5. AFM (a) height and (b) phase images of the PS-PMMA blend. (c) Cross-section measured along the white line in Panel b.

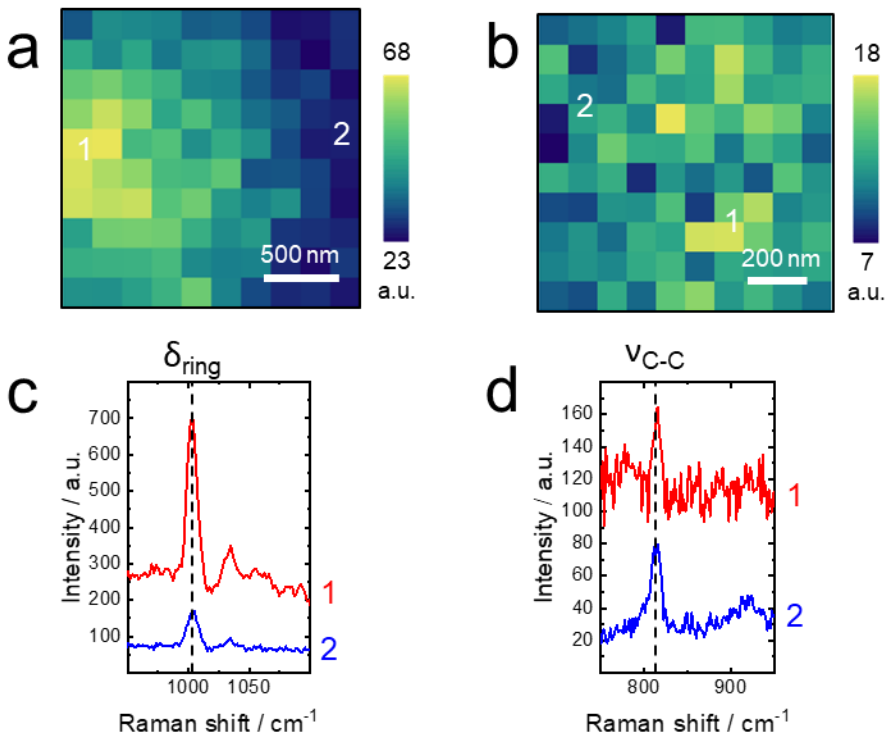

Figure S6. Hotspot images measured at a TERS probe-apex on a pristine (a) PS and (b) PMMA film constructed using the intensity of respective marker bands. (c) PS spectra measured at the hotspot (1) and away from it (2) at the positions marked in (a). (d) PMMA spectra measured at the hotspot (1) and away from it (2) at the positions marked in (b). Spectrum integration time in (a, b) 1s and (c, d) 10 s.

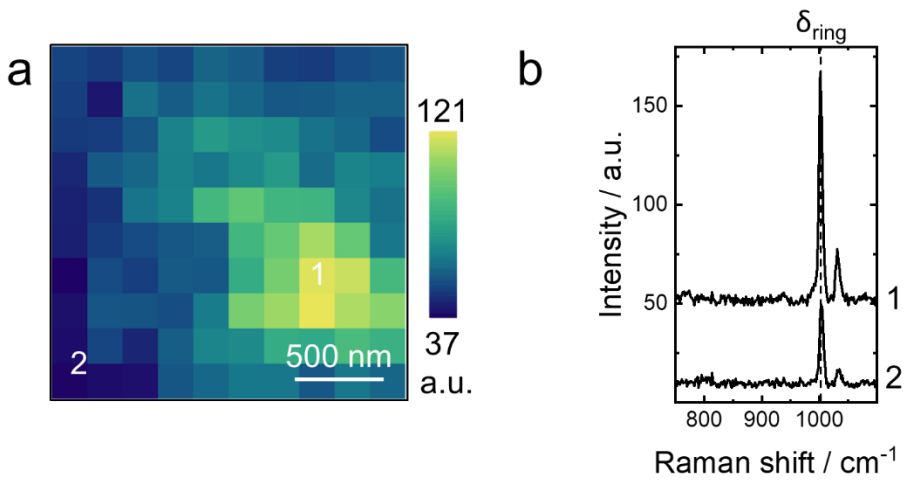

Figure S7. (a) Hotspot image of 1001 cm^{-1} band intensity measured at a TERS probe-apex positioned on the blend surface. Integration time: 1 s. (b) Average spectra recorded at the hotspot and away from it at the positions marked in (a).

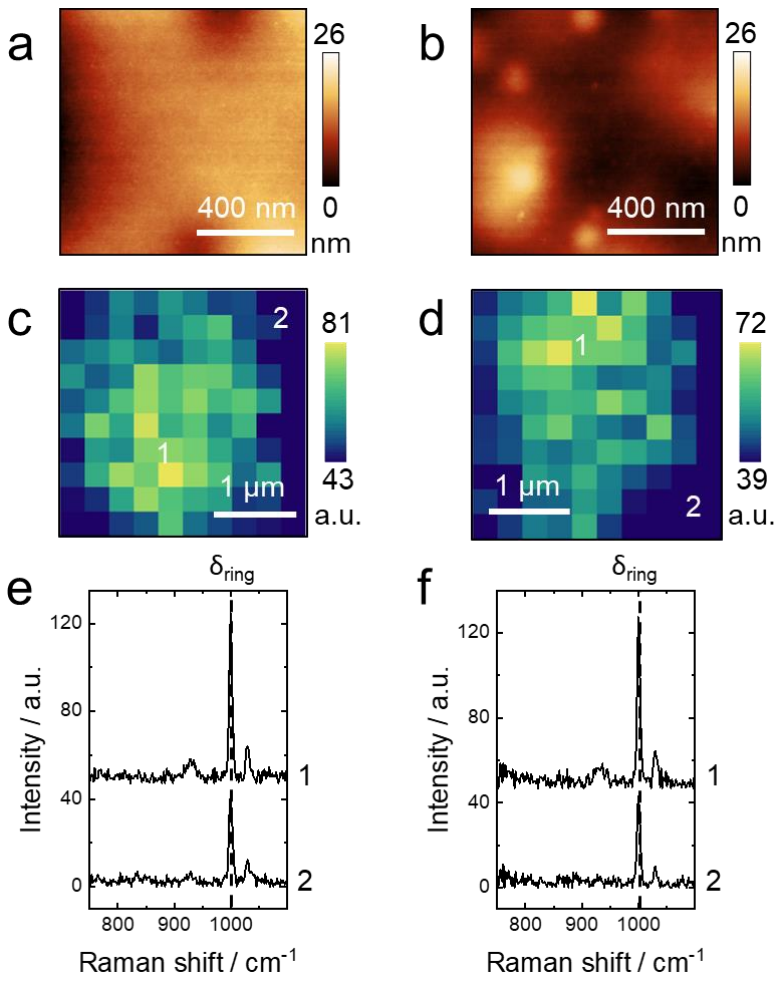

Figure S8. AFM topography images measured in the (a) PS and (b) PMMA domains of the blend. Hotspot images (constructed using the PS signal intensity) measured at the TERS probe-apex inside the (c) PS and (d) PMMA domains shown in (a) and (b), respectively. Spectrum integration time: 1 s. (e) Average of 10 spectra recorded at the hotspot (1) and away from it (2) at the positions marked in (c). (f) (e) Average spectra recorded at the hotspot (1) and away from it (2) at the positions marked in (c).

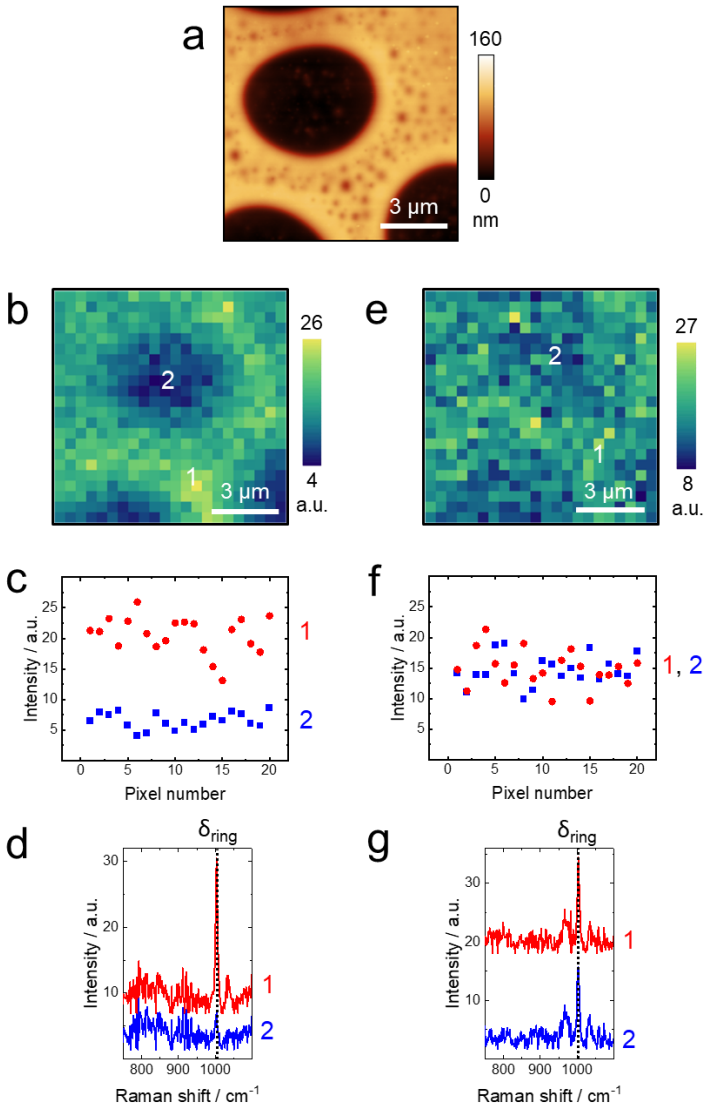

Figure S9. (a) AFM topography image and (b) confocal Raman image of the PS signal intensity measured in the same region of PS-PMMA blend. Spectrum integration time: 1 s. (c) Plot of PS Raman signal intensity recorded at 20 positions within different PS (red) and PMMA (blue) domains identified in (b). (d) Average of 15 confocal Raman spectra of the PS and PMMA domains measured at the positions marked in (b). (e) TERS image of PS signal intensity measured in the same region of blend shown in (a). Spectrum integration time: 1 s. (f) Plot of PS TERS signal intensity recorded at 20 different positions within the PS (red) and PMMA (blue) domains marked in (e). (g) Average of 15 TERS spectra measured at the positions marked in (e).

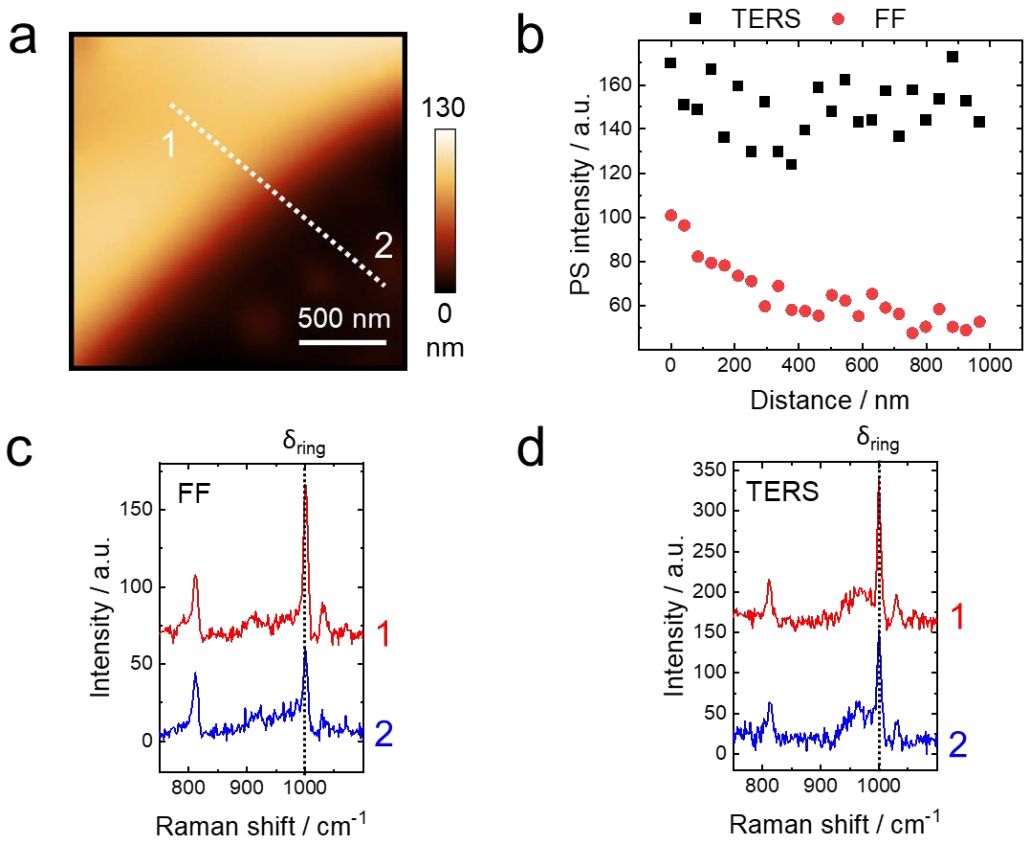

Figure S10. (a) AFM topography image of another domain boundary in PS-PMMA blend. (b) Plots of confocal Raman (CR) and TERS PS signal intensity measured along the line marked in (a). Step size: 42 nm. Averaged (c) confocal Raman and (d) TERS spectra measured in the PS and PMMA domains at the positions marked in (a). Spectrum integration time: 10 s.

Supplementary Note 1: Calculation of TERS information depth

We define TERS information depth as the sample depth from which 95% of the signal originates from. TERS information depth depends on the localized enhancement of electric field (E) at the TERS probe-apex due to the localized surface plasmon resonance (LSPR). LSPR generated *via* interaction of incident laser with the metallic nanostructure located at TERS probe-apex enhances Raman signal intensity with a factor of E^2. Moreover, in the case of small Raman shifts, LSPR also enhances the Raman scattered signal by the same factor, thus leading to an overall signal increase with the factor of E^4.[1] Therefore, TERS enhancement factor (EF) is proportional to the fourth power of local electric field enhancement:

$$EF\alpha\left(\frac{E}{E_0}\right)^4 \quad \text{(S1)}$$

where, E and E_0 are the intensities of electric field in the near-field and the far-field, respectively.

We performed electromagnetic numerical simulations using the geometric model depicted in Figure S10 in Comsol Multiphysics®, a commercial finite-element method solver of Maxwell's equations.[2] The simulation conditions mimicked those used in our TERS experiments. Electric field enhancement of a conical SiO_2/Ag probe with a round apex in contact with PS and PMMA films was simulated. The TERS probe height and angle were set to 450 nm and 45°, respectively. The probe apex diameter was set 50 nm and the Ag coating thickness on SiO_2 tip was set to 100 nm. The polymer thickness was set to 100 nm. Refractive indices of the materials used in the simulations are listed in Table S1. The numerical simulations were carried out with a physics-controlled mesh, which had a minimum size of 0.1 nm between the probe-apex and sample surface. The calculations were simplified by using a plane electromagnetic wave with 532 nm illuminating the TERS probe from the left side. The electric field of this wave was set parallel to the probe plane, thus mimicking the z polarization in the focal spot of a radially polarized excitation laser used in our experiments.[2]

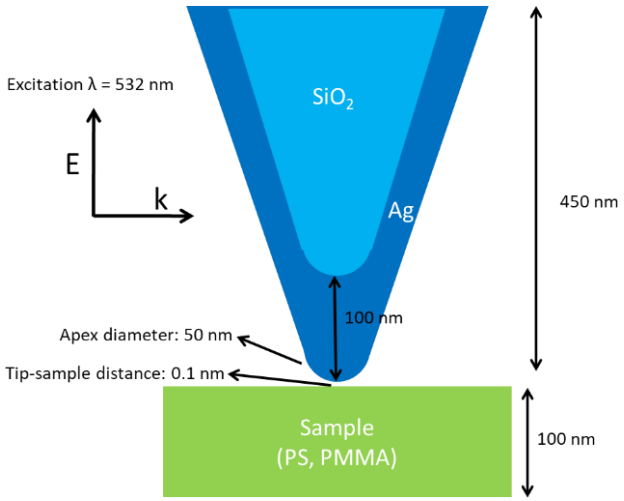

Figure S11. Schematic diagram of the model used in numerical simulations to calculate electric field enhancement at the Ag-coated probe-apex and information depth of TERS within PS and PMMA films.

Table S1. Refractive indices (n + k) of the materials used in numerical simulations.

Material	**n**	**k**
Ag	0.13	3.30
SiO_2	1.45	0
PS	1.59	0
PMMA	1.49	0

Supplementary Note 2: Calculation of XPS information depth

XPS information depth (d) is defined as the sample depth from which 95% of the signal originates from. It is governed by the following equation[3]

$$d = 3\lambda \cos\theta \tag{S2}$$

where, λ is the inelastic mean free path of the electron and θ is the angle between the sample surface normal and the detector collection pathway (emission angle). The XPS setup used in our work operated in normal emission mode, where the sample surface normal and the trajectory of detected electrons are parallel, i.e., θ = 0º. Cumpson estimated λ of PS and PMMA to be 3.2 and 3.1 nm at an electron kinetic energy of 1 keV.[4] Furthermore, at different kinetic energies λ can be determined using the following power-law dependence

$$\lambda_E = \lambda_{1keV}(E)^{0.79} \tag{S3}$$

where, λ_E is the inelastic mean free path of the photoelectron at electron kinetic energy E and λ_{1keV} is the inelastic mean free path of the photoelectron at 1 keV. Kinetic energy of electrons used in our measurement is E = 0.9686 keV.

Using Equations S2 and S3, d for PS and PMMA is estimated to be 9.4 and 9.1 nm, respectively. Assuming λ_{1keV} of PS-PMMA blend is the average of PS and PMMA, d in PS-PMMA blend is estimated to be 9.2 nm.

SUPPLEMENTARY REFERENCES

(1) Hartschuh, A. Tip-Enhanced Near-Field Optical Microscopy. *Angew. Chemie Int. Ed.* **2008**, *47* (43), 8178–8191. https://doi.org/10.1002/anie.200801605.

(2) Kumar, N.; Zoladek-Lemanczyk, A.; Guilbert, A. A. Y.; Su, W.; Tuladhar, S. M.; Kirchartz, T.; Schroeder, B. C.; McCulloch, I.; Nelson, J.; Roy, D.; Castro, F. A. Simultaneous Topographical, Electrical and Optical Microscopy of Optoelectronic Devices at the Nanoscale. *Nanoscale* **2017**, *9* (8), 2723–2731. https://doi.org/10.1039/C6NR09057E.

(3) Schneider, T.; Artyushkova, K.; Fulghum, J. E.; Broadwater, L.; Smith, A.; Lavrentovich, O. D. Oriented Monolayers Prepared from Lyotropic Chromonic Liquid Crystal. *Langmuir* **2005**, *21* (6), 2300–2307. https://doi.org/10.1021/la047788+.

(4) Cumpson, P. J. Estimation of Inelastic Mean Free Paths for Polymers and Other Organic Materials: Use of Quantitative Structure-Property Relationships. *Surf. Interface Anal.* **2001**, *31* (1), 23–34. https://doi.org/10.1002/sia.948.